Emergent Transitions: Discord between Electronic and Chemical Pressure Effects in the *RE*Al_3 (*RE* = Sc, Y, Lanthanides) Series

Amber Lim, Katerina P. Hilleke, and Daniel C. Fredrickson*

Department of Chemistry, University of Wisconsin-Madison, 1101 University Avenue, Madison, Wisconsin 53706, United States

ABSTRACT: Atomic packing and electronic structure are key factors underlying the crystal structures adopted by solid-state compounds. In cases where these factors conflict, structural complexity often arises. Such is born in the series of *RE*Al_3 (*RE* = Sc, Y, lanthanides), which adopt structures with varied stacking patterns of face-centered cubic close packed (FCC, $AuCu_3$ type) and hexagonal close packed (HCP, Ni_3Sn type) layers. The percentage of the hexagonal stacking in the structures is correlated with the size of the rare earth atom, but the mechanism by which changes in size drive these large-scale shifts is unclear. In this Article, we reveal this mechanism through DFT-Chemical Pressure (CP) and reversed approximation Molecular Orbital (raMO) analyses. CP analysis illustrates that the Ni_3Sn structure type is preferrable from the viewpoint of atomic packing, as it offers relief to packing issues in the $AuCu_3$ type by consolidating Al octahedra into columns, which shortens Al-Al contacts while simultaneously expanding the *RE* atom's coordination environment. On the other hand, the $AuCu_3$ type, offers more electronic stability with an 18-*n* closed-shell configuration that is not available in the Ni_3Sn type (due to electron transfer from the *RE* d_{z^2} atomic orbitals into Al-based states). Based on these results, we then turn to a schematic analysis of how the energetic contributions from atomic packing and the electronic structure vary as a function of the ratio of FCC and HCP stacking configurations within the structure and the *RE* atomic radius. The minima on the atomic packing and electronic surfaces are non-overlapping, creating frustration. However, when their contributions are added, new minima can emerge from their combination for specific *RE* radii representing intergrowth structures in the *RE*Al_3 series. Based on this picture, we propose the concept of emergent transitions, within the framework of the Frustrated and Allowed Structural Transitions principle, for tracing the connection between competing energetic factors and complexity in intermetallic structures.

1. INTRODUCTION

Sterics and electronics have long been known to influence the structures of molecular and solid-state compounds.[1-3] In the case of molecules, the ways in which these factors interact are easily understood from experience and well-known models. For example, the preferred number of ligands and trends in the ligand association constants of a transition metal complex can be rationalized by examining the number of valence electrons, degree of orbital overlap, and ligand size.[4] Intermetallic phases comprise a vast family of solid-state compounds in which understanding how such effects underlie observed structures is much more challenging. The extensive range of potential compositions and structure types establishes near-limitless potential for the prediction and discovery of new materials, but models are needed if one is to distinguish between reasonable and unreasonable candidate structures using more than empirical considerations of interatomic distances, radius-ratio trends, or valence electron count.

To address these issues, recent developments in computational chemistry have expanded the chemist's theoretical toolkit. In terms of analyzing bonding and electron structure, the tools include Bader analysis,[5] Crystal Orbital Hamilton Population analysis,[6-8] indicators for electron localization,[9-11] and Wannier functions.[12,13] Meanwhile, empirical considerations of radius-ratio or unit cell volume trends have been supplemented by the DFT-Chemical Pressure (CP) method, which has been applied to describing atomic packing effects in several complex intermetallics.[14-17] The availability of these methods to study packing and electronic effects separately opens opportunities to explore how new phenomena can emerge from their interaction.

In this Article, we consider how conflict between electronic and atomic packing effects begets complexity in a series of *RE*Al_3 (*RE* = Sc, Y, lanthanides) phases, as illustrated by the structure of $HoAl_3$ with c = 35.83 Å (Figure 1). Within this structure, a large repeat vector arises from the interlayering of two parent structures: the $AuCu_3$ type and the Ni_3Sn type. A $AuCu_3$-type *RE*Al_3 phase consists of a corner-sharing network of Al octahedra which interpenetrates a simple cubic network of *RE* atoms (Figure 2, top). A *RE*Al_3 phase adopting the Ni_3Sn type contains face-sharing columns of Al octahedra running along the c axis, which are embedded in a hexagonally close-packed network of *RE* atoms. The $HoAl_3$ structure represents an intergrowth structure in which slabs of the Ni_3Sn type are periodically interrupted by planes of cubic stacking where the $AuCu_3$ structure appears. The *RE*Al_3 series (Figure 2, bottom) traces out the possibilities implied by this arrangement: some adopt the $AuCu_3$ type, the Ni_3Sn type, or form intergrowths like $HoAl_3$. What controls this progression?

Previous synthetic reports show a direct correlation between the percent of hexagonal stacking adopted and the radius of the *RE* atom (Figure 3).[18-20] The $AuCu_3$ type supports a range of metallic radii, from 1.63 Å (Sc) to 1.77 Å (Dy).[19,21-24] Phases with larger *RE* atoms tend to form in the Ni_3Sn type.[18,19,23,25-28] For a narrow range of intermediate *RE* radii, intergrowths of the cubic and hexagonal types form.[19,20,24,29,30] However, the mechanisms by which the atomic sizes direct these structural arrangements remain unclear.

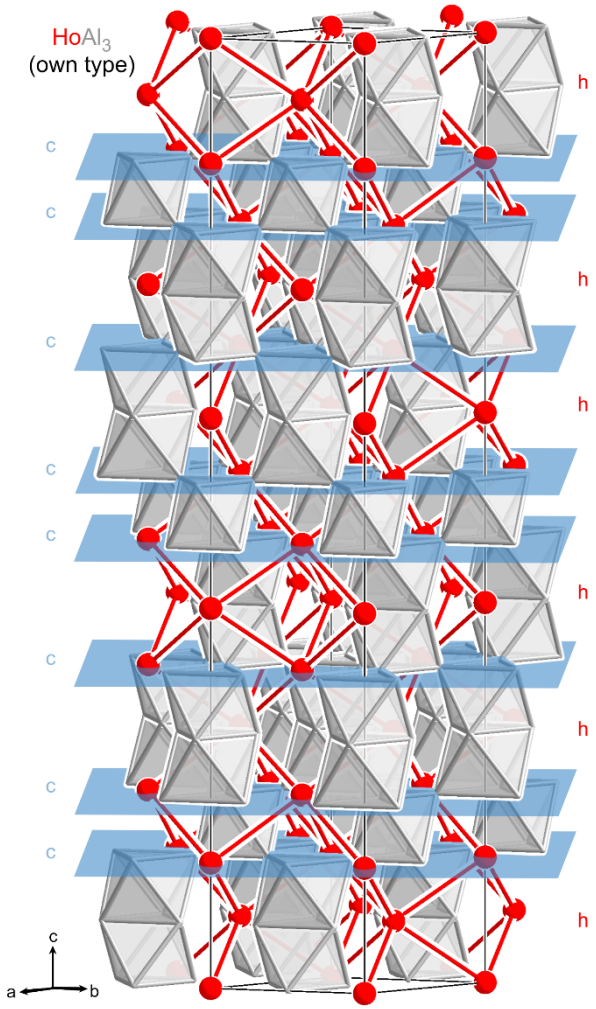

Figure 1. $HoAl_3$ in its own type. Blue planes mark insertion of cubic stacking that periodically interrupt the hexagonal stacking.

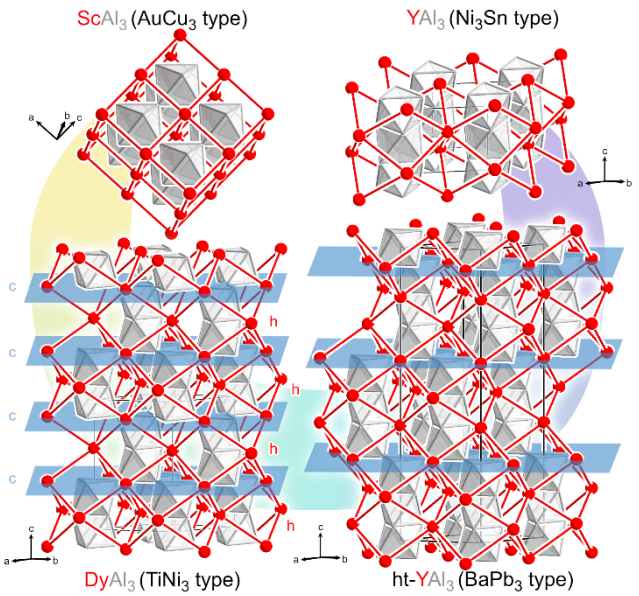

Figure 2. Structural progression across the *RE*Al_3 series. The $AuCu_3$ and Ni_3Sn type represent colored variants of the FCC (*c*) and HCP (*h*) stackings of close-packed layers, while more complex structures, such as the $TiNi_3$ and $BaPb_3$ types, arise from intergrowing these stacking patterns.

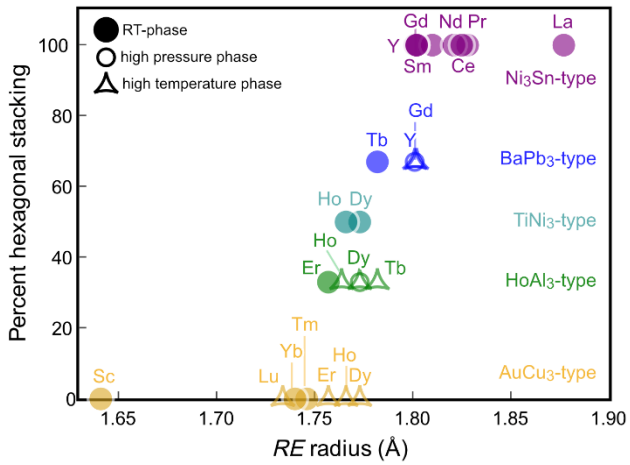

Figure 3. Reported structure types and percent hexagonal stacking in the *RE*Al_3 series as function of the metallic radius of the *RE* atom. High temperature and pressure phases are distinguished with the use of different markers.

An examination of steric factors solely in terms of metallic radii reveals limited information about the forces that act upon each atom. To extract the impact of atomic packing in the local environment, we will use DFT-Chemical Pressure (CP) analysis,[14-17] a theoretical method that allows one to visualize internal tensions imposed by the atomic packing, which are referred to as chemical pressures (CPs). The signs and shapes of the obtained CP lobes reveal sources of packing tension and anticipate how structural changes can exacerbate or soothe those pressures. Using CP analysis, we will examine how *RE* atomic size influences the relative stabilities of the cubic or hexagonal stacking arrangements.

In terms of electronic effects, the *RE*Al_3 series appears to fall within the scope of the 18-*n* bonding scheme, in which a closed-shell configuration on the rare-earth metal is achieved through the covalent sharing of electrons along *RE*-*RE* contacts.[31,32] An analysis using the DFT-reversed approximation Molecular Orbital (DFT-raMO) method[33] will show that picture indeed applies to the $AuCu_3$-type phase. However, it will also become quickly apparent that the bonding scheme for Ni_3Sn phases is much less optimized. In combining these preferences of the atomic packing and electronic contributions to the energy, we will see a frustration arise that leads to emerging minima that are not anticipated by the energetics of either factor alone corresponding to complex intergrowths such as the $HoAl_3$ type. This sets the stage for the concept of emergent transitions, which expands on the general observation that frustrated interactions can give rise to complexity and segregation of different interaction types.

2. EXPERIMENTAL SECTION

2.1. DFT-Chemical Pressure. DFT electronic structures for the generation of CP schemes for $ScAl_3$ and YAl_3 in the $AuCu_3$- and Ni_3Sn-type structures were calculated with the *ABINIT* package.[34-37] Non-spin-polarized LDA-DFT geometry optimizations were performed using Hartwigsen-Goedecker-Hutter norm-conserving pseudopotentials[38,39] first by relaxing the atomic positions in a fixed unit cell, then performing a second calculation in which atomic positions and cell parameters were released simultaneously. After the optimized geometry was obtained, single-point calculations on the structures at their equilibrium volumes and slightly expanded and contracted volumes (linear scale ±0.5%) were performed to extract the kinetic energy, electron densities, and local components of the Kohn-Sham potential for use in creating the CP maps. Calculations were considered converged at an energy difference of 10^{-5} eV between electronic

steps, and when differences in forces were less than 2.6×10^{-3} eV/Å for ionic steps.

To spatially distribute the contributions from the Ewald energy and E_α components, the appropriate number of localized and itinerant electrons was determined through the standard calibration procedure.[17] Auxiliary calculations were carried out on extremely expanded and contracted geometries (linear scale ±20.0%). The number of electrons localized to atomic core regions in these auxiliary calculations were tuned with the *CPpackage* software until all the integrated pressures within the Bader atomic volumes were within 1% of each other. The average of the localized electrons for each atom in the expanded and contracted auxiliary calculations was used for the generation of the CP maps for the equilibrium volume. The CP maps were then constructed using the core-unwarping procedure[15] and the mapping of the nonlocal energy contributions from the atoms to their corresponding regions.[16] The maps were interpreted in terms of interatomic interactions with the Hirshfeld-inspired contact volume scheme,[15] assuming atomic charges ranging from 0% to 100% of those obtained with a Quantum Theory of Atoms in Molecules analysis with the Bader program[40] using free ion electron densities generated with the Atomic Pseudopotentials Engine (APE).[41]

The CP schemes were visualized with the in-house program *figuretool2*. The CP features show similar trends for all assumptions regarding the atomic charges; in the main text, we present the schemes generated assuming the atoms have charges that are 50% of those obtained in the Bader analysis, while results for other assumptions regarding ionicity and further discussion are given in the Supporting Information.

2.2. Electronic Density of States and DFT-raMO analysis. The structures were geometrically optimized using the Vienna ab initio Simulation Package (VASP)[42,43] with the generalized gradient approximation (GGA) and the Projector Augmented Wave (PAW) potentials provided with the package.[44,45] Density of states (DOS) distributions were obtained from single-point calculations on the energy-minimized geometries. Calculations were performed in high-precision mode and considered converged at an energy difference of 10^{-5} eV between electronic steps and 10^{-4} eV between ionic steps. Computational parameters, including k-point meshes, are given in the Supporting Information.

In preparation for the DFT-raMO analysis,[33] separate single-point calculations were run without symmetry considerations to obtain wavefunctions distributed over the whole Brillouin zones. A 3×3×3 k-point mesh was used for the $AuCu_3$ type and a 2×2×4 k-point mesh for the Ni_3Sn type. Wavefunctions from VASP calculations were extracted with the *WaveTrans* program[46]. Using our *DFT-raMO* program, we imported the planewave coefficients for the occupied states and loaded them into a matrix. Separately, atomic target functions were generated from Slater-type orbitals (STOs) which were parameterized to match the radial shapes of the PAW projector functions.[33] The overlap integrals between the occupied crystal orbitals (at the start; remainder states in later steps) and the target STOs were then calculated to generate the raMO Hamiltonian matrix. This raMO matrix was diagonalized at each step to obtain the raMO reconstructions of the targets and remainder functions for use in the next cycle of the process.

In the DFT-raMO analysis of Ni_3Sn-type YAl_3, Sc was substituted for Y in the single-point calculations after geometry optimizations, as the VASP package potential library contains a Sc potential with only the valence 4*s* and 3*d* electrons modeled explicitly but no analogous potential for Y is available. The absence of semicore valence electrons here eliminates radial nodes in the pseudo-wavefunctions that would complicate the raMO projections. To gauge whether this substitution affected relevant details of the electronic structure, band structures of Ni_3Sn-type YAl_3 and Sc-substituted YAl_3 were calculated and compared. As can be seen in Figure S4 in the Supporting Information, this substitution has a negligible impact on the features of the band structure.

3. RESULTS & DISCUSSION

3.1. Chemical Pressure analysis. Empirical data suggests that the structure type adopted by each *RE*Al_3 phase is correlated to the size of the *RE* atom.[18] Compounds with smaller *RE* atoms (i.e. Sc, Tm) adopt the cubic $AuCu_3$ type whereas those with larger *RE* atoms (i.e. La, Nd) assume the hexagonal Ni_3Sn type, with superstructures arising for phases with intermediately sized *RE* atoms (Figure 3). To examine how the size of the *RE* atom drives this progression, we carried out DFT-CP analysis on the two end members of the series: the $AuCu_3$- and Ni_3Sn-types as represented by $ScAl_3$ and YAl_3, respectively. Here, Sc and Y are chosen to represent the *RE* elements since they capture much of the atomic radius range of the relevant *RE* elements and the propensity for the 3+ oxidation states without the complication of having open 4*f* subshells.

CP analysis is a theoretical method that examines packing tensions in solid-state structures. In this approach, the output of DFT calculations is used to resolve the *macroscopic internal pressure* of a structure into a spatially varying map that is interpreted in terms of interatomic pressures (as opposed to external applied pressure). These local pressures, referred to as chemical pressures (CPs), reveal points that would locally prefer expansion or contraction of the geometry but are prevented from doing so by opposing tensions elsewhere, and in this way represent packing frustration.

First, we consider the CP scheme of $AuCu_3$-type $ScAl_3$ (Figure 4a.) The local pressures experienced between the atoms are represented by black and white surfaces drawn around each atom. Black lobes indicate negative pressures, where contraction of the atomic contacts is energetically favorable, and white lobes signify positive pressures, where expansion between contacts could relieve packing tensions. The magnitude of the lobes is proportional to the sum of the pressures experienced by the atom along those directions.

In this case, the Sc atoms (connected by red lines in Figure 4a) are surrounded by nearly spherical white surfaces, indicating that they experience isotropic positive pressures; they are relatively large for their coordination environment and prefer that the structure expand. This is mirrored by the CP surfaces around the Al atoms (gray octahedra), where positive pressures specifically directed toward the Sc atoms appear to constrict the Sc coordination environment. Expansion of the coordination environment is resisted, however, by negative pressures (black) along the Al-Al contacts that show the Al-Al contacts are already overly stretched. Conversely, the Al-Al contacts cannot shorten without further compressing the Sc atom's coordination environment, running up against positive pressures. As such, the CP scheme of $AuCu_3$-type $ScAl_3$ reveals competing packing tensions between the Sc-Al and Al-Al contacts in their preferences for expansion and contraction, respectively.

How would substituting a larger *RE* atom for Sc affect these pressures? The Al sublattice would need to expand to accommodate a larger *RE* atom, but this would be resisted by the negative pressures along overly extended Al-Al contacts. Therefore, larger *RE* atoms in the $AuCu_3$ type would exacerbate the packing tensions at work in $ScAl_3$. Indeed, substitution of Sc with Y to form a hypothetical $AuCu_3$-type YAl_3 phase results in an increase of the Al-Al interatomic distances from 2.84 Å to 2.92 Å (in LDA-DFT optimized geometries). The CP scheme of the hypothetical $AuCu_3$-type YAl_3 has similar features to those seen for $ScAl_3$ (Figure 4a, c), showing the same packing issues.

Inspection of the Ni_3Sn structure type shows how it is poised to relieve much of this packing tension (Figure 2). Condensation of Al octahedra into face-sharing columns creates Al-based regions in

the structure segregated from the *RE* sublattice. This permits the Al-Al contacts to shorten. Indeed, the Al-Al contacts within the octahedra are shortened from 2.92 Å in the $AuCu_3$ type to 2.83 Å and 2.90 Å in Ni_3Sn-type YAl_3.

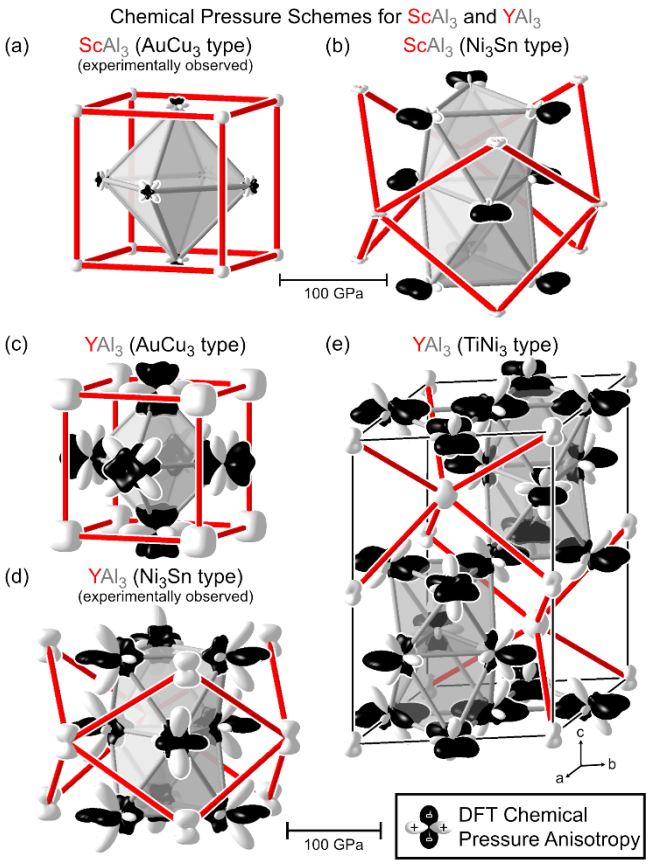

Figure 4. Chemical pressure schemes for (a, b) $ScAl_3$ and (d, e) YAl_3 (d, e) in the $AuCu_3$, and Ni_3Sn structure types, as well as (f) Ti_3Ni-type YAl_3. Cubic $AuCu_3$-type $ScAl_3$ and hexagonal Ni_3Sn-type YAl_3 are experimentally observed, while the other structures are hypothetical. The $TiNi_3$ type is a 1:1 intergrowth of cubic and hexagonal stacking.

Simultaneously, the Al atoms have more freedom to shift away from the *RE* atoms, allowing the restrictive *RE* coordination environment to expand. In the $AuCu_3$ type, all twelve Y-Al contacts are 2.92 Å. In the Ni_3Sn type, the six Y-Al contacts in the *ab* plane are 0.10 Å longer by comparison, providing packing relief from the tighter coordination environment that the *RE* atoms experience in the $AuCu_3$ type. The other six Y-Al contacts around the Y atoms, meanwhile, shorten a minute amount (by 0.01 Å) in the Ni_3Sn type.

A CP analysis of the Ni_3Sn-type YAl_3 affirms this expectation of the packing relief (Figure 4d), as can be seen by comparing the sizes of its lobes with their counterparts for the $AuCu_3$ type (Figure 4c). While the negative pressures on the Al atoms pointing outward from the octahedra to Al neighbors are of similar magnitude to negative pressures in the $AuCu_3$ type, those within the columns are significantly reduced, reflecting the changes seen in interatomic distances. This reduces the negative net CPs on the Al atoms from -15.76 GPa ($AuCu_3$ type) to -12.21 GPa (Ni_3Sn type).[47] The condensation of octahedra into columns thus relieves much of the pressure experienced along the overly stretched Al-Al contacts.

This contraction of the Al octahedra also supports CP relief for the Y atoms via expansion of their coordination environments. Recall that in the $AuCu_3$ type, the Y atom would experience isotropic positive pressures from its 12 nearest-neighbor Al atoms (Figure 4c). In Ni_3Sn-type YAl_3 (Figure 4d), by contrast, Y primarily experiences positive pressure from the Al atoms in the *ab* planes above and below them—these are the six shorter Y-Al distances. The result is an hourglass-shaped CP distribution on Y. Notably, the positive pressures to the atoms above and below are of similar magnitudes as their counterparts in the $AuCu_3$ type, while the remaining pressures in the *ab* plane are significantly reduced as the Al neighbors are shifted away from Y (from 2.92 Å to 3.02 Å) to get closer to other Al atoms within the columns of octahedra. As a result, the net pressure on Y is reduced from +37.41 GPa in the $AuCu_3$ type to +23.94 GPa in the Ni_3Sn type. It is understandable, then, that the Ni_3Sn type becomes increasingly favored for larger *RE* atoms.

As the CP scheme of the $AuCu_3$ type has the same shape of features for both Sc and Y atoms, the Ni_3Sn type should also provide steric relief for *RE*Al_3 phases with smaller *RE* atoms. To investigate this possibility, we performed CP analysis on a hypothetical Ni_3Sn-type $ScAl_3$ structure. In the $AuCu_3$ type, Sc-Al and Al-Al contacts are both 2.84 Å. In moving to the Ni_3Sn type, the stretched Al-Al contacts shorten to 2.75 Å and 2.80 Å within the octahedra, manifesting in the CP scheme as nearly optimized contacts within the Al octahedra (Figure 4b). Meanwhile, the Sc-Al contacts extend to 2.87 Å (out of the *ab* plane) and 2.86 Å (within the *ab* plane), yielding flat, disc-like positive pressure features on the Sc atoms. Though prominent negative CP lobes point outward from the Al columns, there is an overall reduction in the magnitude of the net pressure experienced by them, from -4.20 GPa ($AuCu_3$ type) to -3.18 GPa (Ni_3Sn type).[48] The net atomic CPs on the Sc atoms also decrease from +13.24 GPa to +9.93 GPa. These trends all point to relieved packing tensions in the Ni_3Sn type even with smaller *RE* atoms.

How do these packing effects manifest in the intergrowth structures? To investigate this, we performed CP analysis on an analogous hypothetical $TiNi_3$-type structure (50:50 combination of hexagonal and cubic stacking) for YAl_3, with the metallic radius of Y putting it right on the sharp transition region in Figure 3. In this structure type, Al octahedra occur in face-sharing pairs along the *c* axis, which share corners with other pairs at cubic-type layers. Similarly, the *RE-RE* network alternates between trigonal prismatic and octahedral connectivity (Figure 2).

The CP scheme of $TiNi_3$-type YAl_3 (Figure 4e) resembles a superposition of the CP schemes of the parent structures, with positive Sc-Al CPs being balanced against mostly negative Al-Al pressures. In addition, the strongest Al-Al negative CPs appear where Al octahedra share corners, as in the $AuCu_3$ type, and pointing outwards from the Al octahedra where they share faces, as in the Ni_3Sn type.

Perhaps the largest difference is the decrease in Y CP magnitudes relative to the parent structures. This reduction can be understood from a cooperation among several distortion modes: expansion of the Y coordination environments in the *ab*-plane is supported by the contraction of the triangles shared by the Al octahedra, as in the Ni_3Sn type. The stretching of the Al-Al contacts elsewhere, particularly in the $AuCu_3$-type layers, is then compensated with a compression of the octahedra along the *c*-axis, with the interlayer Al-Al contacts being more optimized in terms of CP than in either parent structure. Note, though, that in obtaining improved Y-Al and inter-

layer Al-Al distances, positive CPs have emerged in the shared Al-triangles, which detract from the stability of the structure. In addition, relatively large Al-Al negative CPs in the $AuCu_3$-type layers point again to the Ni_3Sn type as a more efficient packing.

Overall, our CP analysis of the *RE*Al_3 series reveals packing issues underlying the cubic $AuCu_3$ type that the hexagonal Ni_3Sn type is poised to soothe: positive *RE*-Al CPs that compete directly with negative Al-Al CPs. As the size difference between the *RE* and Al atoms increases, tensions are aggravated and the Ni_3Sn type is expected to be increasingly preferred, in-line with the empirical trends shown in Figure 3. Altogether, these results highlight a fundamental difference in the relationship between the *RE*-Al and Al-Al distances within the two structure types. In the $AuCu_3$ type, the *RE*-Al and Al-Al distances are restrained to be equal due to symmetry considerations. In the Ni_3Sn type, however, the condensation of the Al atoms into columns of octahedra (and the lowered symmetry that results) means that the *RE* coordination environments can expand while *shrinking* many of the Al-Al contacts. An examination of the CP scheme of the 1:1 intergrowth structure, the $TiNi_3$ type, illustrates that this picture extends to the intermediate geometries (particularly for Y, a midsized RE atom), with the introduction of cubic stacking leading to increased negative Al-Al CP.

If hexagonal packing always provides better packing for the series, what favors the formation of the $AuCu_3$ type or the insertion of $AuCu_3$-type layers in an intergrowth? In the next section we will see that the answer lies in the electronic structures of these two structure types.

3.2. Electronic structure analysis. An examination of the *RE*-*RE* connectivity in the *RE*Al_3 phases suggests that both the $AuCu_3$- and Ni_3Sn-type end members may be classified as 18-*n* compounds. In this class of structures, transition metal atoms achieve closed-shell electronic configurations by sharing electrons in multicenter bonding functions, termed *isolobal bonds*.[31] Each isolobal bond corresponds to a covalently shared pair of electrons between two transition metal atoms. The number of isolobal bonds *n* is correlated to the optimal number of valence electrons such that a filled 18-electron configuration on the transition metal is reached at 18-*n* electrons. This approach has been useful for rationalizing a variety of intermetallic systems, including the Nowotny Chimney Ladders,[49] ReAlSi and ReGaSi,[50] $Rh_3Cd_{5-\delta}$ ($\delta \sim 0.56$),[51] $ZrAl_3$,[31] ($CoGa_3$/$IrIn_3$)-type structures,[31,52] and β-$FeSi_2$.[31]

Since the 4*f* orbitals of the lanthanide atoms are highly contracted around their cores, they are not expected to participate significantly in interatomic interactions. As such, the lanthanides bring only their 6*s*, 5*d*, and 6*p* orbitals to the bonding, and they may be considered transition metals within the context of the 18-*n* rule, as was concluded previously for $HoCoGa_5$-type compounds.[53] Each *RE*Al_3 phase has 12 valence electrons per *RE* atom, which gives *n*=6 for the number of nearest-neighbor *RE*-*RE* isolobal bonds needed around each *RE* atom. Indeed, in the $AuCu_3$ type, one *RE* atom is centered in an octahedra of 6 *RE* atoms, while *RE* atoms in the Ni_3Sn type are centered in a trigonal prism of 6 *RE* atoms (Figure 2). With each *RE* atom having 6 *RE* neighbors in both structure types, the *RE*Al_3 series appears to fall under the 18-*n* classification based on geometrical considerations. The resulting closed-shell configurations would then be expected to lead to a pseudogap in the density of states (DOS) distribution near the Fermi energy (E_F). In fact, the DOS curves calculated for both YAl_3 and $ScAl_3$ in the $AuCu_3$ type show this feature, as do those for the $TiNi_3$ type, a half-cubic-half-hexagonal stacking (Figure 5).

However, the situation is less picturesque for the Ni_3Sn-type structures (Figure 5, right). The E_F of Ni_3Sn-type $ScAl_3$ lies on a peak between two minima ca. -7.5 eV and -6.5 eV, while for YAl_3, the E_F falls short of a deep pseudogap at around -6.5 eV, indicating that these compounds have a surplus and deficit of electrons, respectively, relative to the counts needed to achieve a closed-shell configuration. The bonding in Ni_3Sn-type *RE*Al_3 is more complicated than is expected from a cursory counting of *RE*-*RE* contacts.

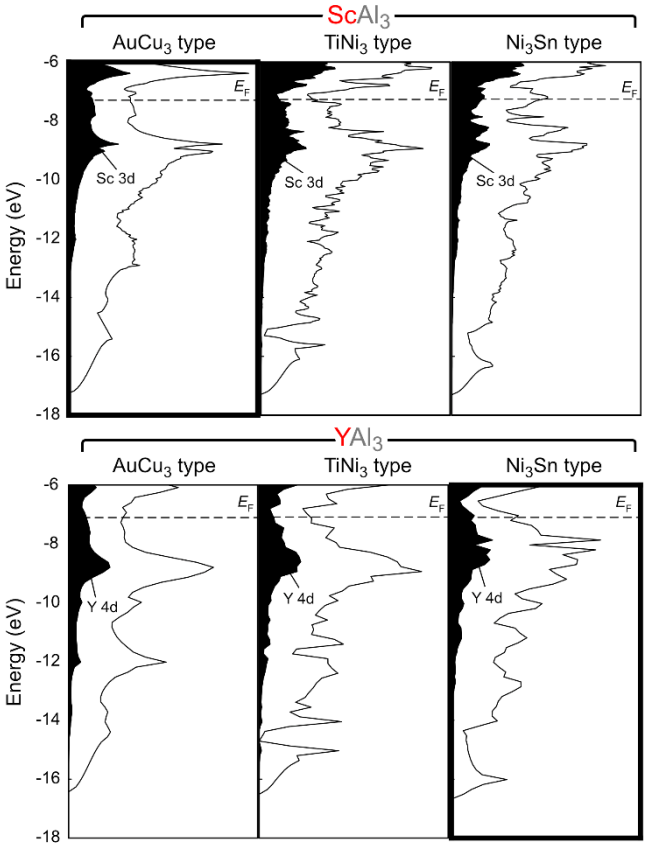

Figure 5. Electronic density of states (DOS) distributions calculated for $ScAl_3$ and YAl_3 in the $AuCu_3$ (0% hexagonal stacking), $TiNi_3$ (50% hexagonal stacking), and Ni_3Sn types (100% hexagonal stacking). The contributions of Sc or Y *d* character to the DOS are shaded. Diagrams for experimentally observed phases are shown with bold outlines.

To explore how the electronic structure of the Ni_3Sn-type members of this series relates to the 18-*n* bonding scheme, we conducted a DFT-reversed approximation Molecular Orbital (DFT-raMO) analysis.[33] The DFT-raMO method is a Wannier-like analysis that reconstructs proposed atomic and molecular orbital-like states (as opposed to maximally localized functions) from the occupied crystal orbitals. Using the set of reconstructed functions (raMOs, each of which account for two electrons in the electronic structure), one can then reinterpret the electronic structure of a system in terms of a local, molecular-style bonding scheme through unitary transformations.[32,54]

In DFT-raMO analysis, we begin with a hypothesis of a local MO diagram that applies to our system, such as a series of electron pairs associated with the atomic orbitals of a central atom. The occupied crystal orbitals in the system of interest form our basis set and are used to reconstruct the hypothesized set of states to the

greatest extent possible while maintaining orthogonality, resulting in raMO functions. The hypothesis is rejected, verified, or modified based on the character of the raMOs with the following standards: (1) the raMOs should be relatively localized, (2) the raMOs should be of similar character to the targeted state, and (3) a majority of the symmetry-related raMOs in the set must be reconstructed with sufficient local character (more on this below). If a set of raMO functions fulfills these requirements, electrons in the system are allocated to those states. Unused remainder states form the basis set for the next round of raMO reconstructions.

To illustrate this process, we begin with a DFT-raMO analysis of $ScAl_3$ in the $AuCu_3$ type, where the DOS distribution affirms its classification as an 18-*n* compound. From the 18-*n* bonding scheme, we expect that each Sc atom participates in six Sc-Sc isolobal bonds, as can be created with a bonding pair of sp^3d^2 hybrid orbitals (derived from the Sc valence *s*, p_x, p_y, p_z, d_z^2, and $d_{x^2-y^2}$ atomic orbitals) along each Sc-Sc contact. The Sc atoms contribute one electron to each of the isolobal bonds around it for a total of 6 electrons per Sc atom. The three unused Sc *d* orbitals then contain the remaining six valence electrons with two electrons each. With this hypothesis as a guide, we start the analysis with a 3×3×3 supercell of $ScAl_3$ (27 formula units with the periodic boundary conditions of a 3×3×3 k-point mesh) and attempt to reconstruct the Sc-Sc isolobal bonds one-by-one from the occupied crystal orbitals.

A challenge in carrying out such a sequence of steps is assessing the quality of the resulting raMO functions to determine whether the reconstructions are successful. One could visually inspect each of the raMO functions, but this is inherently qualitative; it would be challenging to identify subtle trends across a large series of functions (162 for the 3×3×3 supercell of $ScAl_3$). To address this, we introduce a new metric, P_{sphere}, to assist in quickly evaluating trends in the quality of the raMO reconstructions over the course of the sequence.

P_{sphere} is calculated for each raMO function by integrating the electron density within a sphere of defined radius and dividing it by the total electron count in that raMO function. As such, it corresponds to the probability of finding an electron in a raMO within the specified sphere. The sphere radius (r_{sphere}) is chosen to encompass space the target function is expected to occupy (usually to include surrounding atoms that contribute to the bonding).

As we begin to reconstruct the Sc-Sc isolobal bonds, we set r_{sphere} to 2.30 Å from the midpoint of the Sc-Sc contacts to reach the nearest Sc and Al neighbors. An example of the resulting raMO functions is shown in the inset to Figure 6. The reconstructed isolobal bond function appears as a green lobe centered on the Sc-Sc contact, which (at this isosurface level) engulfs a square of Al atoms. The apparent Al contributions to these raMOs affirms the multi-center nature of the isolobal bond. At the bottom of Figure 6, we plot the P_{sphere} values for the Sc-Sc isolobal bond functions (raMOs 1-81) with blue markers. P_{sphere} begins at 0.8 and stays consistently above 0.6 throughout the 81 possible Sc-Sc isolobal bonds (3×3×3 supercell with 3 isolobal bonds per unit cell). The downward trend in the P_{sphere} values across the series is expected, as when shared crystal orbital character is utilized in earlier functions, it is unavailable to the later ones. The shapes of the raMOs are also qualitatively consistent throughout. Accordingly, 162 of the 324 valence electrons available in the supercell are assigned to the Sc-Sc isolobal bonds. In terms of one $ScAl_3$ formula unit, this corresponds to 6 of the 12 electrons belonging to the Sc-Sc isolobal bonds.

Next, the Sc atomic orbitals d_{xy}, d_{xz}, and d_{yz} are reconstructed, where we expect to find two electrons per *d*-orbital. In the generat ed raMOs, the appropriate *d*-like lobes are centered on the Sc atoms. Additionally, at the corner of each lobe, the function is decorated with the back lobes of *p*-like bonding contributions from the Al neighbors (Figure 6, inset). As shown for each set of *d* orbitals with green, red, or purple markers in Figure 6, the first 24 of the 27 functions in the supercell have P_{sphere} (r_{sphere} = 3.00 Å) values above 0.4, after which P_{sphere} sharply drops to values under 0.1. Inspection of the last raMOs shows delocalization and Al *p* character instead of the proposed *d*-based functions (Figure S7). These functions are thus not classified as occupied Sc *d*-based orbitals and are returned to the basis set of remainder states, as indicated with open markers. Accordingly, each of these Sc *d* orbitals is allocated 1.78 electrons (24/27 *d*-raMOs × 2 electrons per raMO = 1.78 electrons per Sc).

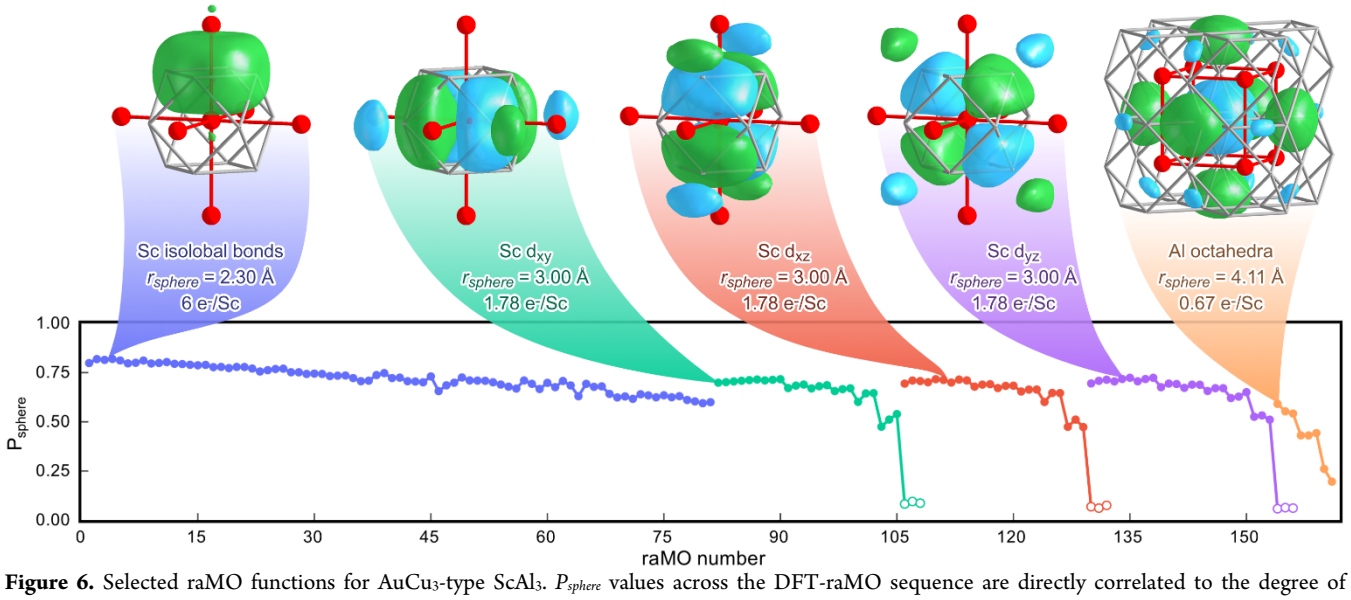

Figure 6. Selected raMO functions for $AuCu_3$-type $ScAl_3$. P_{sphere} values across the DFT-raMO sequence are directly correlated to the degree of localization of the raMO function. The radius r_{sphere} is chosen such that it encompasses space where the functions are expected to occupy. Open markers for P_{sphere} indicate raMO functions that are not allocated electrons due to their low P_{sphere} value and irrelevant orbital character; they were returned to the basis set of remainder states.

Full occupation of the Sc d_{xy}-, d_{xz}-, and d_{yz}-based functions would correspond to completion of the 18-electron configurations we expected from the pseudogap at the E_F. Where are the remaining 0.67 electrons? The rejected raMOs in the sequence above give hints here. The rejected raMOs from the Sc *d*-states have Al *p* character localized to Al-rich regions, suggesting the remaining electrons are associated with Al-based functions. Based on this observation, we next attempt to construct raMOs centered in Al octahedra, away from the Sc atoms. The resulting raMOs indeed are centered within Al octahedra with significant Al *p* character (Figure 6 inset). With r_{sphere} set to 4.11 Å, P_{sphere} drops from 0.59 to 0.20 across the raMOs (Figure 6, orange markers), yet inspection of the raMOs with lower P_{sphere} values continues to show relatively localized functions centered within Al octahedra (Figure S8) until there are no more electrons left to account for. Thus, the remaining 0.67 electrons per Sc are allocated to Al-Al bonding functions.

The DFT-raMO bonding scheme is a close match to the proposed 18-*n* configuration. Six electrons participate in the isolobal bonds, while approximately two electrons are contained in each of the remaining Sc *d* atomic orbitals. A small number of electrons are drawn away from the t_{2g} Sc *d* orbitals by Al_6 *s*-like cage orbitals, but this is a tractable perturbation on the 18-*n* bonding scheme. Hence, the E_F for $AuCu_3$-type $ScAl_3$ lies in a pseudogap.

We now consider how this situation changes on going to YAl_3 in the Ni_3Sn type. To start, we reconstruct the raMOs in an analogous sequence to that of the $AuCu_3$-type structure, using a 2×2×4 super cell (32 formula units of YAl_3). First, the 96 proposed Y-Y isolobal bonds are reconstructed (3 per formula unit), which in the coordinate system of the structure, involves the Y valence *s*, p_x, p_y, p_z, d_{xz}, and d_{yz}. As shown in the leftmost raMO function in Figure 7, the function rests between two Y atoms and encompasses a rectangle of Al atoms, evidence that the orbitals from Al contribute to the multicenter bonding. Initial P_{sphere} values (r_{sphere} = 2.30 Å) for these raMOs (shown in blue) hover around 0.70 for most of the sequence but drop to approximately 0.25 in the last few raMO functions. Visual inspection of these last raMOs shows the expected orbital characteristics despite some delocalization (Figure S9), so electrons are assigned to all 96 states for a total of 192 electrons out of the 384 available valence electrons, or 6 of the 12 valence electrons per Y atom.

Next, we reconstruct two of the remaining three Y orbitals, $d_{x^2-y^2}$ and d_{xy}. As with the $AuCu_3$ type, the presence of Al character on the reconstructions of the *RE* atom's *d* orbitals is suggestive of significant *RE*-Al interactions (Figure 7 inset, green, red). P_{sphere} values for both sets of *d*-based raMOs remain above 0.25 for 31 out of 32 raMOs, equating to 1.94 electrons per Y for each *d*-based orbital (31/32 raMOs × 2 electrons per raMO).

Finally, we turn to the Y d_{z^2} atomic orbitals, which prove more difficult to reproduce. The first Y d_{z^2} raMOs in the sequence adopt a delocalized, columnar shape: the d_{z^2} character of the central atom is apparent but involves bonding contributions from the d_{z^2} orbitals of the neighboring Y atoms along the *c* axis (Figure 7 inset, purple).

After continuing further in the series, the P_{sphere} values drop significantly after the first half of the set, implying that these orbitals account for one electron per Y atom. Therefore, the order of the Y d_{z^2} raMOs is chosen such that every other Y site in the *c*-direction was targeted. P_{sphere} (r_{sphere} = 3.10 Å) drops significantly past the 16th raMO. Continuing past this point yields raMOs with no apparent Y d_{z^2} character and significantly delocalized isosurfaces centered in the columns of Al (Figure S10). Therefore, only about one electron per Y atom can be assigned to Y d_{z^2} states (16/32 raMOs × 2 electrons per raMO). This, combined with the shape of the raMOs, where d_{z^2} character is spread across Y atoms above and below the target site, shows that Y achieves some Y-Y bonding in these half-

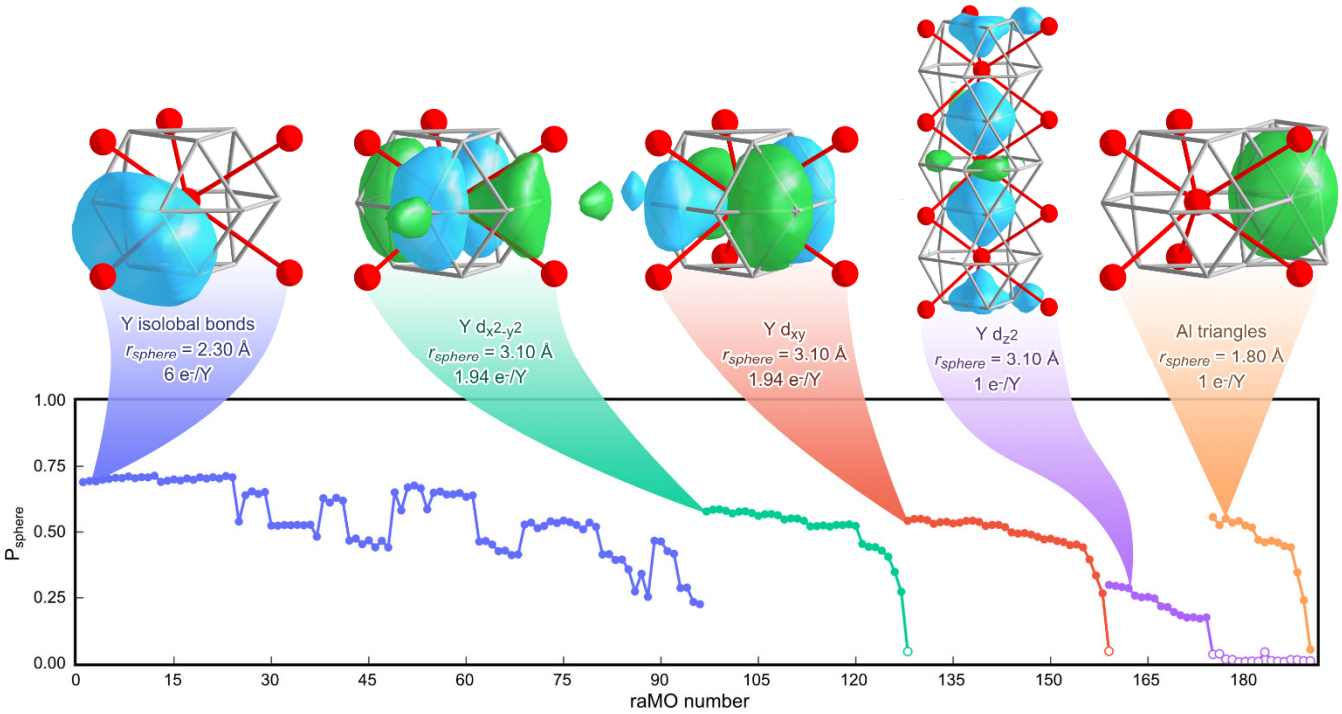

Figure 7. Selected raMO functions and P_{sphere} values across the Ni_3Sn-type YAl_3 DFT-raMO scheme. Open circles that occur after steep drops in P_{sphere} values indicate that we assign no electrons to the corresponding raMOs.

filled states beyond that expected from our initial geometry inspection. Additionally, bridging Al atoms contribute character across these Y-Y interactions, creating chains of delocalized isolobal bonding. With this, we have accounted for 11 of 12 electrons per Y atom.

Let's find the last electron. In the rejected Y d_z^2 raMO functions (Figure S10), we observed significant Al character centered within the columns of Al octahedra. This leads us to our next hypothesized state in the raMO model. As highlighted in orange in Figure 7, this state is centered on shared triangular faces between Al octahedra. As we expect to see some delocalization akin to that of the Y d_z^2 raMOs, we'll start by reconstructing bonding orbitals at every other shared face. The resulting raMOs amount to 2 electrons per 2 Al octahedra or 1 electron per Al octahedron. Though the drop in P_{sphere} (r_{sphere} = 1.80 Å) in the last few raMOs demonstrates significant delocalization, the raMOs maintain the expected character. Therefore, the last remaining electron is allocated to states centered within the columns of Al octahedra.

Why do we see this partial filling of the Y d_z^2 and Al-based states in the Ni_3Sn type? The sterically motivated consolidation of Al octahedra into face-sharing columns in the Ni_3Sn type creates regions dense with Al-Al interactions, creating low-lying bonding functions. The Y d_z^2 states are perfectly poised for the transfer of electrons to these Al-based functions, as the Y d_z^2 orbitals may overlap along *c* and share electrons among multiple Y atoms. One electron is redistributed from the Y d_z^2 state to the Al-based states, yielding essentially a half-filled d_z^2 band for each column of Y atoms along *z*. This situation for the Y d_z^2 orbitals is analogous to a classic model system for band structures, the chain of equally spaced H 1*s* orbitals whose bonding is optimized at a half filling (before a band gap is opened by a Peierls distortion). In a sense, the chain of Y atoms can effectively be considered as adding 1 to the count of *n* isolobal bonds in the 18-*n* rule.

With the Y d_z^2 and Al octahedra both having partially filled levels, it is not surprising that no pseudogap is evident at the E_F for the Ni_3Sn type. The nearest pseudogap instead appears in the range of 12.5 to 13 electrons per formula unit. As is shown in the Supporting Information, a raMO analysis including all the crystal orbitals up to 13 electrons per Y atom reveals that the additional electrons needed to reach this DOS feature further populate the Al-based states to 2 electrons per Al octahedron.

The filling of 13 electrons per formula unit is compatible with the 18-*n* rule, when we consider the presence of valence electrons not associated with the *RE* atoms. The full electron count is then given by 18-*n*+*m*, where *m* is the number of electrons per *RE* atom in states associated with just the Al atoms.[31] The Y atoms reach 18-*n* configurations with *n* = 7 at 11 electrons per Y atom, while *m* = 2 is required for the Al-based bonding functions (3-center 2-electron bonds in the shared Al_3 triangles within the columns of face-sharing octahedra). A closed-shell configuration is then achieved at 18-7+2 = 13 electrons per Y atom. At 12 electrons per formula unit, YAl_3 is electron poor relative to this bonding scheme.

This picture helps rationalize several earlier observations regarding Ni_3Sn-type structures. The minima in the DOS distributions for this type coincide with electron counts greater than 12 electrons per formula unit. Indeed, there are reports of Ni_3Sn-type *RE*Al_3 with Ge and Si partial substitution,[55-57] as well as the high pressure 14-electron compounds $BaSn_3$, $EuGe_3$, and $BaGe_3$.[58-60]

3.3. Emergent intergrowths in the *RE*Al_3 series. Earlier, we saw that the Ni_3Sn type offers a more favorable atomic packing arrangement than the $AuCu_3$ type. These electronic features bring to the foreground the advantages that the $AuCu_3$ type confers: a more optimal bonding scheme with greater separation between filled and empty electronic levels. The relative importance of these two factors is determined by the size of the *RE* atoms. This can be seen in the comparison of $ScAl_3$ and YAl_3. The total energy of $AuCu_3$-type $ScAl_3$, where the Sc represents the smallest *RE* atom, is 0.19 eV per formula unit lower than that of the hypothetical Ni_3Sn-type form. In comparison, the total energy for Ni_3Sn-type YAl_3, where the *RE* atom is considerably larger, is 0.02 eV per formula unit lower than the $AuCu_3$ type. We can infer that the relief of chemical pressure provided by the Ni_3Sn type for larger *RE* atoms overcomes the energetic costs of the less optimized electronic structure. Intergrowths of cubic and hexagonal stacking arise at intermediate *RE* atomic sizes.

The emergence of the intergrowth structures in this series can be interpreted in terms of the Frustrated and Allowed Structural Transitions (FAST) principle.[61] Within this scheme, one envisions the possible structures that can be constructed from a parent structure through conceptual transformations among real and hypothetical structures (and not necessarily to physical processes governed by kinetics). When different energetic factors disagree on the favorability of the transition to a new structure (*frustrated transitions*), one can expect that this transition will not be competitive compared to another transition where those factors agree (*allowed transitions*). At first glance the *RE*Al_3 series appears to represent a case of frustration: the atomic packing and electronic components are always in conflict with each other, meaning that no transition between any of the *RE*Al_3 structures would be allowed.

This is illustrated qualitatively at the top of Scheme 1 with schematic plots of a structure's energy as a function of the *RE* atom radius and the ratio of hexagonal (Ni_3Sn type) vs. cubic ($AuCu_3$ type) stacking sequences. We start in the upper left with the atomic packing component. In our CP analysis, Ni_3Sn type provides steric relief for *RE* atoms of all sizes, but the effect is much more pronounced for larger *RE* atoms. This can be represented with an energy minimum (dark color) in the large radius, 100% hexagonal corner.[62] The energy increases as cubic stacking is introduced, and the surface becomes shallower as the *RE* atoms become smaller. We can represent the electronic component of the energy with a similar energy surface (Scheme 1, upper right). The $AuCu_3$ type achieves greater separation between filled and unfilled states, providing electronic stability regardless of the *RE* atomic size. This results in an energy surface that slopes down towards structure types with more cubic packing.

Even with these qualitative plots, an important consequence of their form can be seen when we add the energetic contributions of the components together (Scheme 1, bottom left). The minimum of the summed surface is in the upper right region at large *RE* radii and 100% hexagonal packing. Spanning out from the minimum, the contours take on an elliptical shape where the upper section curves lean towards the minima, while the lower section begins to uncurl as *RE* radius becomes smaller.

We can understand implications of this shape by taking constrained paths along *y* at fixed *RE* radii, as shown with dashed lines labeled with a, b, and c (Scheme 1, bottom right). Phases with smaller *RE* atoms (curve a) are the lowest energy with no hexago-

nal stacking (i.e. $AuCu_3$-type $ScAl_3$), while phases with larger *RE* atoms (curve c) adopt the lowest energy configuration with pure hexagonal stacking (i.e. Ni_3Sn-type YAl_3). However, something new happens for phases with intermediately sized *RE* atoms: on curve b, the minimum lies between 0% and 100% hexagonal stacking, echoing intergrowth structures observed for intermediate *RE* atom sizes.

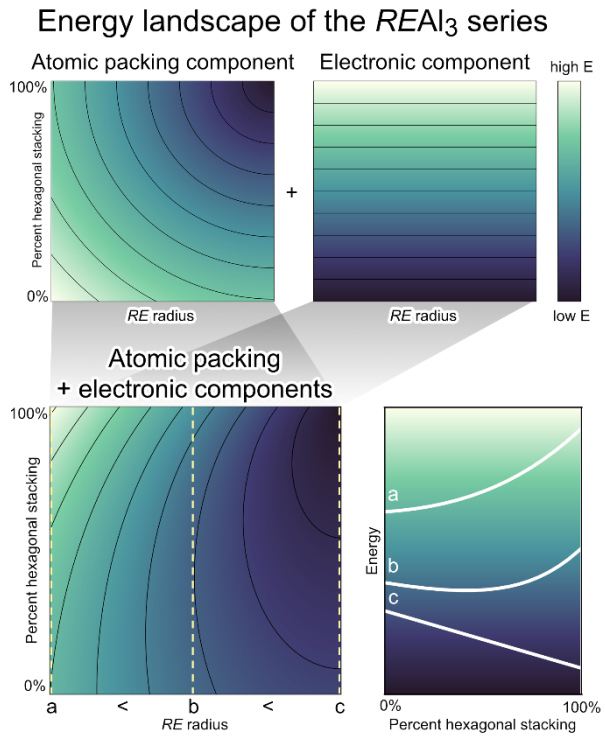

Scheme 1. The qualitative energy surfaces for the atomic packing and electronic components of the $REAl_3$ series as a function of RE radius size and percent hexagonal stacking, shown separately (top) and as a sum (bottom). Energy curves for specific RE radii (corresponding to the dashed lines a, b, and c on the summed surface) are plotted in the lower right.

The local minimum at this intermediate *RE* atomic size is not present in either of the atomic packing or electronic maps, but rather, emerges from their combination. In this *emergent transition*, the minima from the contributing components are misaligned, such that their sum creates new local minima at intermediate regions for particular *RE* atomic sizes. The appearance and position of these emergent local minima depend on the relative weights of the contributing surfaces.

How do emergent transitions relate to the FAST principle? In frustrated and allowed structural transitions, the maxima or minima of the separate components are envisioned to overlap on the combined energy surface, canceling each other out or deepening the energy surface. In this case, however, there are no points in which low energy regions or valleys on the two separate surfaces overlap to form a deepened minimum. Instead, new valleys emerge from the atomic packing and electronic surfaces sloping in opposite directions along *y*.

4. CONCLUSIONS

In this Article, we have examined the factors underlying the structural preferences in the $REAl_3$ series, which stretches from the simple $AuCu_3$-type for small *RE* atoms, through a series of complex intergrowth structures for somewhat larger *RE* atoms, to the Ni_3Sn type for the largest *RE* atoms. Using DFT-CP analysis, we uncovered how consolidation of Al into columns of octahedra in the hexagonal Ni_3Sn-type end-member releases compression of larger *RE* atoms that occur in the $AuCu_3$ type while relieving some stretched contacts between Al atoms. This is half of the story behind the structural transition. DFT-raMO analysis (with the aid of the newly developed P_{sphere} tool) shows that the Ni_3Sn type introduces partially filled Y d_z^2 and Al-based states, disrupting the closed-shell configuration that provides electronic stability to the $AuCu_3$ type. This results in the mismatch between the E_F and a pseudogap in the DOS distributions of the Ni_3Sn-type structures.

Based on this picture, qualitative predictions can be made about how the $REAl_3$ structures can evolve under the application of high pressure or high temperature. Of the two endmembers, the $AuCu_3$-type exhibits a higher density (as can be understood from the Ni_3Sn-type being adopted to attain a more open *RE* coordination environment). $AuCu_3$-type features would then be expected to be more favorable under applied pressure.

In terms of temperature, we would expect the structure with more vibrational freedom to be increasingly favored as the temperature is raised. This can be judged from the quadrupolar character of the CP features of the atomic sites, high values of which are connected to modes of soft atomic motion.[63] The quadrupolar character, as measured by the recently developed QP metric,[64] is significantly higher for Al atoms in the $AuCu_3$ type than in Ni_3Sn type (see Table 1), consistent with the *d*-orbital like shape of the Al CP features in the former. This suggests that higher temperatures would tend to enhance the $AuCu_3$-type features of a structure. The test predictions are validated in Figure 3 where the structure types of high-temperature and high-pressure phases are marked with open circles and triangles respectively. In fact, for all cases, the high-temperature and high-pressure phases show decreased hexagonal stacking character than their ambient temperature/pressure analogues.[24,25]

Table 1. Chemical Pressure quadrupole metric values (QP)

Compound	QP (RE)[a]	QP (Al)
$ScAl_3$ ($AuCu_3$ type)	0.000	0.777
$ScAl_3$ (Ni_3Sn type)	0.121	0.360
YAl_3 ($AuCu_3$ type)	0.000	0.826
YAl_3 (Ni_3Sn type)	0.106	0.473

[a] $QP = \frac{(\sum_m c_{l=2,m}^2)}{\sum_{l=0}^{l_{max}=6} \sum_m c_{l,m}^2}$ where $c_{l,m}$ is the coefficient of the $Y_{l,m}(\theta,\phi)$ spherical harmonic contributing to the $CP(\theta,\phi)$ distribution for the given atom.

The competition between electronic and atomic packing effects creates a series of intergrowths between the two parent structure types through the phenomenon of emergent transitions. With larger *RE* atoms, packing tensions drive the structures toward steric relief in the form of increased hexagonal stacking, despite the electronic stability provided by the 18-*n* configuration of the $AuCu_3$ type. The summation of the misaligned electronic and atomic packing components forms a discontinuous energy landscape where minima emerge at various percentages of hexagonal stacking at intermediate *RE* sizes.

We look forward to exploring how other structural phenomena fall within the framework of emergent transitions. Potential examples from the literature include the rich family of superstructures that arise from competition between steric and electrostatic effects in stuffed CoSn-type phases,[65] as well as the compromise between packing and bonding requirements in Sr*RE*Ga_3O_7 that underlie a 3×3×1 superstructure of melilite.[66] Beyond this, we are interested in applying the concept of emergent transitions to the design of intergrowth systems. To do this, one can select two crystal structures that are related by some perturbation, such as a stacking variation, that optimize different aspects of the bonding at the expense of others. By performing elemental substitutions that shift the relative importance of those factors, scenarios analogous to that shown in Scheme 1 could be created, opening avenues to the discovery of new structural complexity.

ASSOCIATED CONTENT

The Supporting Information is available free of charge at http://pubs.acs.org.

Additional computational details, CP schemes at generated with differing ionicities levels, selected CP schemes generated with semicore *RE* pseudopotentials, comparison of LDA and PBE CP schemes for $ScAl_3$, band structure comparisons of Ni_3Sn-type YAl_3 and Sc-substituted YAl_3, band structure and density of states of $LaAl_3$, selected DFT-raMO functions for $ScAl_3$ ($AuCu_3$) YAl_3 (Ni_3Sn), DFT-raMO scheme of 13-electron YAl_3, and DOS distribution of YAl_3 (Ni_3Sn) showing hypothetical electron counts. (PDF)

AUTHOR INFORMATION

Corresponding Author

Daniel C. Fredrickson – *Department of Chemistry, University of Wisconsin-Madison, Madison, Wisconsin, United States*; orcid.org/0000-0002-3717-7008; Email: danny@chem.wisc.edu.

Authors

Amber Lim – *Department of Chemistry, University of Wisconsin-Madison, Madison, Wisconsin, United States*; orcid.org/0000-0001-9893-1740

Katerina P. Hilleke – *Department of Chemistry, University of Wisconsin-Madison, Madison, Wisconsin, United States*

Present address: *Department of Chemistry, State University of New York at Buffalo, Buffalo, New York, USA*; orcid.org/0000-0003-4322-8403

ACKNOWLEDGMENT

We gratefully acknowledge the financial support of the National Science foundation through Grant DMR-2127349. This research used computational resources supported by NSF grant CHE-0840494.

REFERENCES

(1) Mizutani, U. Hume-Rothery Rules for Structurally Complex Alloy Phases; CRC Press, 2011.
(2) Frank, F. C.; Kasper, J. S. Complex Alloy Structures Regarded as Sphere Packings. I. Definitions and Basic Principles. *Acta Crystallogr.* **1958**, *11*, 184-190.
(3) Frank, F. C.; Kasper, J. S. Complex alloy structures regarded as sphere packings. II. Analysis and classification of representative structures. *Acta Crystallogr.* **1959**, *12*, 483-499.
(4) Cotton, F. A.; Wilkinson, G. *Advanced Inorganic Chemistry*; Wiley, 1988.
(5) Bader, R. F. W. *Atoms in Molecules: A Quantum Theory*; Oxford University Press, 1994.
(6) Dronskowski, R.; Bloechl, P. E. Crystal Orbital Hamilton Populations (COHP): Energy-resolved Visualization of Chemical Bonding in Solids Based on Density-functional Calculations. *J. Phys. Chem.* **1993**, *97*, 8617-8624.
(7) Deringer, V. L.; Tchougreeff, A. L.; Dronskowski, R. Crystal Orbital Hamilton Population (COHP) Analysis as Projected from Plane-wave Basis Sets. *J. Phys. Chem. A* **2011**, *115*, 5461-5466.
(8) Maintz, S.; Deringer, V. L.; Tchougreeff, A. L.; Dronskowski, R. Analytic Projection from Plane-wave and PAW Wavefunctions and Application to Chemical-bonding Analysis in Solids. *J. Comput. Chem.* **2013**, *34*, 2557-2567.
(9) Becke, A. D.; Edgecombe, K. E. A simple measure of electron localization in atomic and molecular systems. *J. Chem. Phys.* **1990**, *92*, 5397-5403.
(10) Kohout, M. A measure of electron localizability. *Int. J. Quantum Chem* **2004**, *97*, 651-658.
(11) Wagner, F. R.; Kohout, M.; Grin, Y. Direct Space Decomposition of ELI-D: Interplay of Charge Density and Pair-Volume Function for Different Bonding Situations. *J. Phys. Chem. A* **2008**, *112*, 9814-9828.
(12) Wannier, G. H. The Structure of Electronic Excitation Levels in Insulating Crystals. *Phys. Rev.* **1937**, *52*, 191-197.
(13) Marzari, N.; Mostofi, A. A.; Yates, J. R.; Souza, I.; Vanderbilt, D. Maximally localized Wannier functions: Theory and applications. *Rev. Mod. Phys.* **2012**, *84*, 1419-1475.
(14) Fredrickson, D. C. DFT-Chemical Pressure Analysis: Visualizing the Role of Atomic Size in Shaping the Structures of Inorganic Materials. *J. Am. Chem. Soc.* **2012**, *134*, 5991-5999.
(15) Berns, V. M.; Engelkemier, J.; Guo, Y.; Kilduff, B. J.; Fredrickson, D. C. Progress in Visualizing Atomic Size Effects with DFT-Chemical Pressure Analysis: From Isolated Atoms to Trends in AB_5 Intermetallics. *J. Chem. Theory. Comput.* **2014**, *10*, 3380-3392.
(16) Hilleke, K. P.; Fredrickson, D. C. Discerning Chemical Pressure Amidst Weak Potentials: Vibrational Modes and Dumbbell/Atom Substitution in Intermetallic Aluminides. *J. Phys. Chem. A* **2018**, *122*, 8412-8426.
(17) Lu, E. D.; Van Buskirk, J. S.; Cheng, J. X.; Fredrickson, D. C. Tutorial on Chemical Pressure Analysis: How Atomic Packing Drives Laves/Zintl Intergrowth in K_3Au_5Tl. *Crystals* **2021**, *11*, 906.
(18) van Vucht, J. H. N.; Buschow, K. H. J. The structures of the rare-earth trialuminides. *J. Less-Common Met.* **1966**, *10*, 98-107.
(19) van Vucht, J. H. N.; Buschow, K. H. J. On binary aluminium-rich compounds of the rare earth elements. *Philips Res. Rep.* **1964**, *19*, 319-322.
(20) Buschow, K. H. J.; van Vucht, J. H. N. Systematic Arrangement of the Binary Rare-Earth-Aluminum Systems. *Philips Res. Rep.* **1967**, 233-245.
(21) Zalutskii, I. I.; Kripyakevich, P. I. RAl_3 compounds in rare earth-aluminum systems and their crystal structures. *Sov. Phys. Crystallogr.* **1967**, *12*, 341-343.
(22) Jones, T. I.; Norlock, L. R.; Boucher, R. R. Some Observations on Aluminum-Thulium Alloys. *J. Less-Common Met.* **1963**, *5*, 128-133.
(23) Kripyakevich, P. I.; Zalutskii, I. I. Compounds of rare-earth metals with aluminum and their crystal structures. *Voprosy Teorii i Primeneniya Redkozem Metal., Akad. Nauk SSSR* **1964**, 144-145.
(24) Cannon, J. F.; Hall, H. T. Effect of high pressure on the crystal structures of lanthanide trialuminides. *J. Less-Common Met.* **1975**, *40*, 313-328.
(25) Bailey, D. M. The structure of two polymorphic forms of YAl_3. *Acta Crystallogr.* **1967**, *23*, 729-733.
(26) Buschow, K. H. J. Phase relations and intermetallic compounds in the systems neodymium-aluminium and gadolinium-aluminium. *J. Less-Common Met.* **1965**, *9*, 452-456.
(27) Kripyakevich, P. I.; Zalutskii, I. I. A new compound in the system cerium-aluminium. *Dopovidi Akademii Nauk Ukrains'koi RSR* **1965**, *1*, 54-56.
(28) Buschow, K. H. J. The Lanthanum-Aluminium system. *Philips Res. Rep.* **1965**, *20*, 337-348.
(29) Baenziger, N. C.; Hegenbarth, J. J. Gadolinium and dysprosium intermetallic phases. III. The structures of Gd_3Al_2, Dy_3Al_2, Gd_5Ge_3, Dy_5Ge_3 and $DyAl_3$. *Acta Crystallogr.* **1964**, *17*, 620-621.
(30) Kripyakevich, P. I.; Zalutskii, I. I. Crystal structure of the compound $TbAl_3$. *Ann. Univ. Mariae Curie-Sklodowska* **1964**, *19*, 97-103.
(31) Yannello, V. J.; Fredrickson, D. C. Generality of the 18-*n* Rule: Intermetallic Structural Chemistry Explained through Isolobal Analogies to Transition Metal Complexes. *Inorg. Chem.* **2015**, *54*, 11385-11398.
(32) Yannello, V. J.; Kilduff, B. J.; Fredrickson, D. C. Isolobal analogies in intermetallics: the reversed approximation MO approach and applications to $CrGa_4$- and Ir_3Ge_7-type phases. *Inorg. Chem.* **2014**, *53*, 2730-2741.

(33) Yannello, V. J.; Lu, E.; Fredrickson, D. C. At the Limits of Isolobal Bonding: π-Based Covalent Magnetism in Mn_2Hg_5. *Inorg. Chem.* **2020**, *59*, 12304-12313.
(34) Gonze, X. A brief introduction to the ABINIT software package. *Z. Kristallogr. - Cryst. Mater.* **2005**, *220*, 558-562.
(35) Gonze, X.; Amadon, B.; Anglade, P. M.; Beuken, J. M.; Bottin, F.; Boulanger, P.; Bruneval, F.; Caliste, D.; Caracas, R.; Côté, M.; et al. ABINIT: First-principles approach to material and nanosystem properties. *Comput. Phys. Commun.* **2009**, *180*, 2582-2615.
(36) Gonze, X.; Beuken, J. M.; Caracas, R.; Detraux, F.; Fuchs, M.; Rignanese, G. M.; Sindic, L.; Verstraete, M.; Zerah, G.; Jollet, F.; et al. First-principles computation of material properties: the ABINIT software project. *Comput. Mater. Sci.* **2002**, *25*, 478-492.
(37) Gonze, X.; Jollet, F.; Abreu Araujo, F.; Adams, D.; Amadon, B.; Applencourt, T.; Audouze, C.; Beuken, J. M.; Bieder, J.; Bokhanchuk, A.; et al. Recent developments in the ABINIT software package. *Comput. Phys. Commun.* **2016**, *205*, 106-131.
(38) The LDA-HGH combination is the platform on which the CP method was originally developed. CP schemes generated with the PBE-HGH pseudopotentials (Krack, M. Pseudopotentials for H to Kr optimized for gradient-corrected exchange-correlation functionals. *Theor. Chem. Acc.* **2005,** *114,* 145-152) for selected systems are provided in the Supporting Information for comparison.
(39) Hartwigsen, C.; Goedecker, S.; Hutter, J. Relativistic separable dual-space Gaussian pseudopotentials from H to Rn. *Phys. Rev. B* **1998**, *58*, 3641-3662.
(40) Henkelman, G.; Arnaldsson, A.; Jónsson, H. A fast and robust algorithm for Bader decomposition of charge density. *Comput. Mater. Sci.* **2006**, *36*, 354-360.
(41) Oliveira, M. J. T.; Nogueira, F. Generating relativistic pseudo-potentials with explicit incorporation of semi-core states using APE, the Atomic Pseudo-potentials Engine. *Comput. Phys. Commun.* **2008**, *178*, 524-534.
(42) Kresse, G.; Furthmüller, J. Efficient iterative schemes for ab initio total-energy calculations using a plane-wave basis set. *Phys. Rev. B: Condens. Matter* **1996**, *54*, 11169-11186.
(43) Kresse, G.; Furthmüller, J. Efficiency of ab-initio total energy calculations for metals and semiconductors using a plane-wave basis set. *Comput. Mater. Sci.* **1996**, *6*, 15-50.
(44) Blochl, P. E. Projector augmented-wave method. *Phys. Rev. B: Condens. Matter* **1994**, *50*, 17953-17979.
(45) Kresse, G.; Joubert, D. From ultrasoft pseudopotentials to the projector augmented-wave method. *Phys. Rev. B* **1999**, *59*, 1758-1775.
(46) *WaveTrans: Real-space wavefunctions from VASP WAVECAR file* 2022. https://www.andrew.cmu.edu/user/feenstra/wavetrans/ (accessed 2022-05-31).
(47) The numerical values of the CPs can vary depending on the assumptions regarding charges and the treatment of the $E_{Ewald} + E_{\alpha}$ terms. However, comparisons of values between similar structures containing the same elements can be made when the same procedure is used for preparing both schemes.
(48) The reduction in the net CP magnitude may be visually unintuitive here, but it can be understood with the limited solid angle covered by negative CP features, with the rest of the angular range being dominated by positive pressure.
(49) Lu, E.; Fredrickson, D. C. Templating Structural Progessions in Intermetallics: How Chemical Pressure Directs Helix Formation in the Nowotny Chimney Ladders. *Inorg. Chem.* **2019**, *58*, 4063-4066.
(50) Decocq, V.; Gui, X.; Neeson, A.; Xie, W.; Heitmann, T.; Wang, F. Crystal Structures, Superconducting Properties, and the Coloring Problem in ReAlSi and ReGaSi. *Inorg. Chem.* **2020**, *59*, 17310-17319.
(51) Koley, B.; Roy, N.; Harshit; Mallick, S.; Simonov, A.; Jana, P. P. A Vacancy-Driven Intermetallic Phase: $Rh_3Cd_{5-\delta}$ ($\delta \sim 0.56$). *Inorg Chem* **2021**, *60*, 5488-5496.
(52) Verchenko, V. Y.; Tsirlin, A. A. Semiconducting and Metallic Compounds within the $IrIn_3$ Structure Type: Stability and Chemical Bonding. *Inorg. Chem.* **2022**, *61*, 3274-3280.
(53) Engelkemier, J.; Green, L. M.; McDougald, R. N.; McCandless, G. T.; Chan, J. Y.; Fredrickson, D. C. Putting $ScTGa_5$ (T = Fe, Co, Ni) on the Map: How Electron Counts and Chemical Pressure Shape the Stability Range of the $HoCoGa_5$ Type. *Cryst. Growth Des.* **2016**, *16*, 5349-5358.
(54) Park, S. W.; Hosono, H.; Fredrickson, D. C. Cation Clustering in Intermetallics: The Modular Bonding Schemes of CaCu and Ca_2Cu. *Inorg. Chem.* **2019**, *58*, 10313-10322.
(55) Zhuravleva, M. A.; Rangan, K. K.; Lane, M.; Brazis, P.; Kannewurf, C. R.; Kanatzidis, M. G. Flux synthesis, structure and physical properties of new pseudo-binary $REAl_{3-x}Ge_x$ compounds. *J. Alloys Compd.* **2001**, *316*, 137-145.
(56) Xia, S.-Q.; Lins, D.; Bobev, S. $SmAl_{2.64(4)}Ge_{0.36(4)}$, with the hexagonal Ni_3Sn structure type. *Acta Crystallogr. Sect. Sect. E: Struct. Rep. Online* **2005**, *62*, i10-i12.
(57) Murav'eva, A. A.; Zarechnyuk, O. S.; Gladyshevskii, E. I. The systems Y-Al-Si (Ge, Sb) in the range 0-33.3 at. % Y. *Inorg. Mater.* **1971**, *7*, 34-36.
(58) Fässler, T. F.; Kronseder, C. $BaSn_3$: A Superconductor at the Border of Zintl Phases and Intermetallic Compounds. Real-Space Analysis of Band Structures. *Angew. Chem. Int. Ed.* **1997**, *36*, 2683-2686.
(59) Castillo, R.; Baranov, A. I.; Burkhardt, U.; Grin, Y.; Schwarz, U. Triangular Ge_3 Units in a New Modification of $EuGe_3$. *Z. Anorg. Allg. Chem.* **2015**, *641*, 355-361.
(60) Fukuoka, H.; Tomomitsu, Y.; Inumaru, K. High-pressure synthesis and superconductivity of a new binary barium germanide $BaGe_3$. *Inorg. Chem.* **2011**, *50*, 6372-6377.
(61) Mitchell Warden, H. E.; Fredrickson, D. C. Frustrated and Allowed Structural Transitions: The Theory-Guided Discovery of the Modulated Structure of IrSi. *J. Am. Chem. Soc.* **2019**, *141*, 19424-19435.
(62) The energy surface for the atomic packing component was calculated by linearly increasing the energy as a function of distance to the upper right corner. The energy surface of the electronic component was calculated as a function of distance to the *x*-axis. The combined atomic packing and electronic component energy surface was calculated as a weighted sum of 65% of the atomic packing component and 35% of the electronic component.
(63) Engelkemier, J.; Fredrickson, D. C. Chemical Pressure Schemes for the Prediction of Soft Phonon Modes: A Chemist's Guide to the Vibrations of Solid State Materials. *Chem. Mater.* **2016**, *28*, 3171-3183.
(64) Kamp, K. R.; Fredrickson, D. C. A Tour of Soft Atomic Motions: Chemical Pressure Quadrupoles Across Transition Metal–Main Group 1:2 Structure Types. *Chem. Mater.* **2022**, *34*, 10011-10024.
(65) Fredrickson, D. C.; Lidin, S.; Venturini, G.; Malaman, B.; Christensen, J. Origins of Superstructure Ordering and Incommensurability in Stuffed CoSn-Type Phases. *J. Am. Chem. Soc.* **2008**, *130*, 8195-8214.
(66) Genevois, C.; Bazzaoui, H.; Boyer, M.; Ory, S.; Ledemi, Y.; Messaddeq, Y.; Pitcher, M. J.; Allix, M. Emergence of A-Site Cation Order in the Small Rare-Earth Melilites $SrRECa_3O_7$ (*RE* = Dy–Lu, Y). *Inorg. Chem.* **2021**, *60*, 12339-12354.

For Table of Contents Use Only

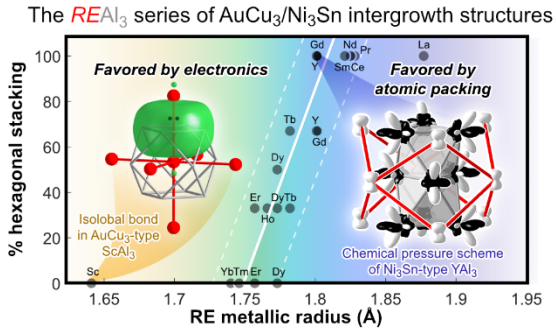

Synopsis: Atomic packing and electronic structure are key factors underlying the structures adopted by solid-state compounds. We reveal how conflict between them leads to a series of superstructures in the *RE*Al$_3$ (*RE* = Sc, Y, lanthanides) phases. A schematic analysis of their individual energetic contributions shows their combination leads to structural possibilities not anticipated by either map alone. Based on this picture, we propose the concept of emergent transitions for the design of complex structures.